J Adv Ceram

Research Article

Phonon and bandgap engineering-driven Y-doped $Mg_2Al_4Si_5O_{18}$ ceramics for high-performance radiative cooling

Di Wu[1,2,3,4], Mohan Zhang[1,3], Xin Wang[1,2,3,4], Ting Wang[1,3], Jiaxin Ye[1,2,3,4], Liyan Xue[1,3,5], Minzhong Huang[1,3,5], Meng Zhang[1,3,5], Fan Yang[1,3,5,6,7]✉, Huimin Xiang[8]✉, Heng Chen[1,3,5]✉

Cite this article: Wu D, Zhang M, Wang X, et al. *J Adv Ceram* 2026, **15**(5): 9221292. https://doi.org/10.26599/JAC.2026.9221292

ABSTRACT: Passive radiative cooling (PRC) is a promising way to alleviate the global energy crisis by reflecting sunlight and dissipating heat through the atmospheric transparent window (ATW). Despite possessing a wide bandgap and complex phonon modes, the PRC performance of $Mg_2Al_4Si_5O_{18}$ is limited by phonon-polariton resonance. Herein, phonon engineering is integrated with bandgap engineering to design and synthesize a series of $Mg_2Al_4Si_5O_{18}$:xY^{3+} (x = 0%, 2.5%, 5%, 7.5%, and 10%) ceramics with excellent PRC performance. Density functional theory (DFT) identifies that Y^{3+} doping effectively suppresses phonon-polariton resonance and widens the bandgap, synergistically enhancing the PRC performance. The as-prepared samples exhibit high ATW emissivity (94.39%–98.39%) and high reflectivity (89.52%–94.77%) in the 0.4–2.5 μm range. Furthermore, the "cooling glass" coating successfully achieves a maximum temperature reduction of 16.5 °C and an average net radiative cooling power of 113.1 W·m^{-2}. Y^{3+} doping enhances ATW emissivity by inducing lattice distortion, which reduces symmetry and alters the dipole moment while boosting reflectivity in the visible and near-infrared (vis-NIR) regions by preserving the wide bandgap through the introduction of optically inert elements. This work synergistically integrates the advantages of high performance, low cost, and environmental friendliness, offering a highly promising ceramic material solution for large-scale radiative cooling applications.

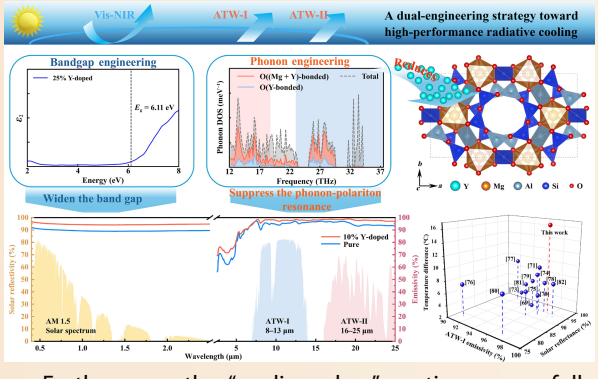

KEYWORDS: passive radiative cooling (PRC); phonon and bandgap engineering; Y-doping β-$Mg_2Al_4Si_5O_{18}$; dual-selective atmospheric transparent window emissivity; visible and near-infrared reflectivity

1 Introduction

Against the backdrop of global efforts toward "carbon peaking" and "carbon neutrality," coupled with the escalating cooling demands of data centers, conventional cooling technologies have emerged as a bottleneck to sustainable development due to their substantial energy consumption and excessive CO_2 emissions [1,2]. To mitigate these environmental concerns, there is an urgent demand for sustainable and environmentally friendly cooling technology. Passive radiative cooling (PRC) technology has recently attracted significant attention due to its zero-energy consumption [3,4] and exhibits potential for applications in building energy conservation [5,6], vehicle thermal management [7], electronic device thermal management [8], spacecraft thermal management [9], and space data centers. Ideal radiative cooling materials should exhibit excellent reflectance in the effective solar radiation band (0.4–2.5 μm) to minimize solar heat absorption while simultaneously possessing high emissivity in both the first atmospheric transparent window (ATW-I; 8–13 μm) and the second atmospheric transparent window (ATW-II; 16–25 μm) [10] to facilitate efficient thermal radiation dissipation into outer space [11,12]. Most existing radiative cooling designs primarily focus on the main ATW-I (8–13 μm), while the cooling potential of the ATW-II (16–25 μm) is often overlooked. It is crucial to note that the atmospheric transparency of ATW-II decreases with increasing humidity due to strong absorption by water vapor,

[1] State Key Laboratory of Structure Chemistry, Fujian Institute of Research on the Structure of Matter, Chinese Academy of Sciences, Fuzhou 350002, China. [2] College of Chemistry and Materials Science, Fujian Normal University, Fuzhou 350117, China. [3] Xiamen Key Laboratory of Rare Earth Photoelectric Functional Materials, Xiamen Institute of Rare Earth Materials, Xiamen 361021, China. [4] Fujian College, University of Chinese Academy of Sciences, Fuzhou 350002, China. [5] Fujian Province Joint Innovation Key Laboratory of Fuel and Materials in Clean Nuclear Energy Systems, Fujian Institute of Research on the Structure of Matter, Chinese Academy of Sciences, Fuzhou 350002, China. [6] China Rare Earth Group Innovation Technology Co., Ltd., Guangdong 518000, China. [7] China Rare Earth Group Research Institute, Shenzhen, Guangdong 518000, China. [8] School of Materials Science and Engineering, Zhengzhou University, Zhengzhou 450001, China.

✉ Corresponding authors. E-mail: F. Yang, fanyang2013@fjirsm.ac.cn; H. Xiang, hmxiang@alum.imr.ac.cn; H. Chen, xmchenheng@fjirsm.ac.cn

Received: February 9, 2026; Revised: April 5, 2026; Accepted: April 6, 2026

making its radiative cooling effect particularly significant in arid climates [10]. Among the current radiation cooling materials, ceramic materials (e.g., Al_2O_3 [13], SiO_2 [14], and MgO [15]) exhibit distinct advantages due to their excellent thermal stability, wide bandgap, and strong molecular vibrations [16,17]. However, the application of certain materials containing precious metals (In [18] and Ag [19]) in the PRC is limited due to high costs and sustainability issues. Consequently, researchers have begun to explore eco-friendly ceramic materials composed of low-cost, earth-abundant elements.

Among potential ceramic materials, $Mg_2Al_4Si_5O_{18}$, possessing a β-cordierite structure, is theoretically predicted to be a promising PRC material. Jing *et al.* [20] calculated the band structure and determined a band gap of 5.098 eV, which is well above the upper boundary of the photon energy in the solar spectrum (4.13 eV). The high bandgap results in the low absorption of solar photons, which makes excellent visible and near-infrared (vis-NIR) reflection capability possible. Furthermore, the phonon density of states (PDOS) analysis conducted by Li *et al.* [21] demonstrates that Al and Si atoms exhibit abundant vibrational modes within the ATW, establishing the fundamental basis for their infrared radiative properties. However, $Mg_2Al_4Si_5O_{18}$ exhibits strongly polarized vibrational bonds, leading to a major impedance mismatch with air (termed phonon-polariton resonance) and a significant reduction in emissivity [22]. Similar limitations have also been reported in other PRC ceramics, such as Al_2O_3 and SiO_2 [2], highlighting the challenge of balancing solar reflectivity and ATW emissivity in single-phase materials. To date, the radiative cooling potential of $Mg_2Al_4Si_5O_{18}$ remains unexplored.

Ion doping emerges as a reliable strategy to mitigate the aforementioned limitations [23–29]. The regulatory effect on the optical and thermal properties of matrix materials has been well validated by extensive research [30,31]. For instance, Wang *et al.* [32] prepared cordierite glass-ceramics, increasing the whole-band normal-direction radiance from 82% to 91% by doping with Fe^{3+}. Therefore, the radiation performance was improved due to lattice distortion and the effect of defects induced by ion doping. It has been confirmed that ion doping can effectively enhance infrared emission performance. However, the transition metal ions were hindered by inherent d–d transitions and charge transfer transitions [33–35], leading to absorption characteristics in the vis-NIR, thereby limiting the solar reflectance [36]. Consequently, identifying a dopant capable of simultaneously suppressing phonon-polariton resonances while preserving a wide bandgap represents a formidable challenge. To circumvent this limitation, rare-earth elements have garnered attention as superior dopants owing to their distinct electronic configurations [37–39]. Y^{3+} is a frequently utilized doping element in rare-earth elements owing to its moderate ionic radius and comparatively low cost [40,41]. On the one hand, the Y^{3+} ion does not undergo any electronic transitions within the 4f configuration and is therefore regarded as optically inactive [42]. This characteristic is pivotal for achieving high reflectivity and maintaining a wide bandgap. On the other hand, the introduction of Y^{3+} disrupts long-range lattice order through mass mismatch and bond distortion, inducing local field inhomogeneity [43]. Structural disorder effectively suppresses narrowband resonance reflection. Consequently, it broadens the emission bandwidth without compromising the absorption intensity, leading to a significant enhancement in radiative performance for ATW applications.

To meet the aforementioned requirements of suppressed phonon-polariton resonance and a wide bandgap, we combine phonon engineering with bandgap engineering to design and synthesize a dual-selective all-inorganic material that exhibits a high vis-NIR reflectance of 94.77%, a high ATW-I emissivity of 97.53%, and a high ATW-II emissivity of 98.39%. Inspired by the concept of "cooling glass" [44], we fabricated the functional coating by mixing low-melting-point glass and $Mg_2Al_4Si_5O_{18}$:10% Y^{3+} into a slurry, followed by coating onto a stone slab and a subsequent thermal treatment. Density functional theory (DFT) calculations demonstrate the feasibility of Y^{3+} doping, and a systematic investigation has been conducted on its influence on the crystal structure, phase composition, vis-NIR reflectance, and ATW emittance of $Mg_2Al_4Si_5O_{18}$. The practical cooling tests indicate that the radiative cooling coating achieved a maximum temperature reduction of 16.5 °C, yielding an average net cooling power of 113.1 $W{\cdot}m^{-2}$. These results indicate that rare-earth modification presents a promising pathway for developing high-performance, environmentally benign, cost-effective, and robust ceramic-based radiative cooling materials.

2 Experimental

2.1 Materials and methods

Commercially available MgO, SiO_2, AlOOH, and Y_2O_3 powders (99.9%, Aladdin Biochemical Technology Co., Ltd., China) were employed as raw materials. The MgO, AlOOH, SiO_2, and Y_2O_3 compounds were precisely weighed according to the stoichiometric ratio and homogenized via planetary ball milling for 6 h using ethanol as the milling medium. The as-mixed powders were uniaxially pressed into green bodies and sintered at 1400 °C for 4 h in air. Then, the sintered powders were subjected to wet ball milling for 24 h, followed by drying at 80 °C, yielding fine $Mg_2Al_4Si_5O_{18}$:xY^{3+} (x = 0%, 2.5%, 5%, 7.5%, 10%, and 12.5%) powders with a uniform particle size distribution.

To evaluate the PRC performance of ceramics, low-melting-point glass particles with controlled particle size and density were employed. Ceramic powder and glass microspheres were mixed at a mass ratio of 7 : 3.5 mL of anhydrous ethanol was added, and the mixture was stirred at 500 r/min for 20 min to ensure thorough and uniform dispersion of the powder (to prevent particle settling or agglomeration). The prepared coating was applied to 6 cm × 6 cm rock plates, dried in a 50 °C oven for 2 h, and then sintered at 870 °C in air for 15 min to obtain the coated samples.

2.2 Characterizations

X-ray diffraction (XRD) analysis was performed using an instrument (Miniflex 600, Rigaku, Japan) with a Cu Kα source at λ = 1.5406 Å. Crystal structure parameters were determined via Rietveld refinement (GSAS II) based on the obtained XRD patterns. Transmission electron microscope (TEM; FEI Tecnai F20, Thermo Fisher Scientific, USA) and an energy dispersive spectroscope (EDS; Talos F200x, Super X, USA) were employed to investigate the microstructure and elemental distribution. The vibrational absorption of functional groups within the structure was characterized using a Raman spectrometer (Horiba LabRAM, Horiba, Japan). Emissivity in the mid-infrared region was measured using a Fourier transform infrared spectrometer (FTIR; Nicolet iS50R, Thermo Fisher Scientific, USA) equipped with a gold-coated integrating sphere (L1272405, PIKE Technologies, USA) and the reflectance method. A zinc selenide window served as the measurement aperture.

Thermogravimetric (TG) analysis and differential scanning calorimetry (DSC) were performed using a simultaneous thermal analyzer (TGA/DSC3+, METTLER TOLEDO, Switzerland). Before testing, the UV–vis-NIR spectrophotometer (Carry 5000,

Agilent, USA) was calibrated using the polytetrafluoroethylene standard to ensure accurate reflectance measurements. Additionally, powder samples were prepared with a uniform particle size to ensure consistent measurement. Additionally, powder samples were compacted into dedicated trays before testing to minimize the light scattering effect on measurements.

The tests were performed at the rooftop of Xiamen Institute of Rare Earth Materials, China (geographic coordinates: 24°32′ N, 118°04′ E; altitude ≈ 32 m) during the summer solstice period (June–July) under typical subtropical climate conditions with an average daily solar irradiance above 850 $W{\cdot}m^{-2}$. The prepared radiative cooling slab was placed inside the central cavity (6 cm × 6 cm × 5 cm) of a high-density expanded polystyrene (EPS) foam enclosure (external dimensions: 120 cm × 60 cm × 30 cm, thermal conductivity ≤ 0.032 $W{\cdot}m^{-1}{\cdot}K^{-1}$). To mitigate parasitic solar absorption and reduce conductive heat influx from the environment, the exterior of the foam enclosure was fully clad with polished aluminum foil exhibiting a solar reflectance exceeding 95%. Temperature monitoring was achieved using a calibrated K-type thermocouple (accuracy ±0.1 °C) connected to a multichannel data acquisition system (Agilent 34972A, Agilent, USA). The thermocouple was positioned at the geometric center of the cavity, maintaining a 5 mm separation from both the inner wall of the foam enclosure and the surface of the slab to avoid conductive thermal artifacts. The cavity aperture was hermetically sealed with a 2 mm-thick high-transmittance polyethylene (PE) film, which served as a protective barrier against ambient airflow while preserving the radiative exchange pathway between the slab and outer space.

Control measurements were performed simultaneously using an identical foam box without the radiative cooling slab to account for background thermal effects, ensuring the reliability of the cooling performance evaluation.

2.3 Computational methods

DFT calculations were performed using the Vienna *Ab initio* Simulation Package (VASP) [45]. For the electronic exchange-correlation energy, the Perdew–Burke–Ernzerhof (PBE) functional within the generalized gradient approximation (GGA) was selected, and the projector-augmented wave (PAW) pseudopotential was employed. All calculations used a 3 × 3 × 3 Monkhorst-Pack *k*-space grid with an energy cutoff of 550 eV. Atomic positions and lattice constants were fully relaxed until the following convergence criteria were met: a total energy difference of less than 1×10^{-8} eV per atom and a maximum ionic force below 0.0005 $eV{\cdot}Å^{-1}$. The phonon spectrum of the systems was calculated using the phonopy package based on density-functional perturbation theory (DFPT) [46]. The second-order interatomic force constants were determined using a 2 × 2 × 2 supercell. The optical properties of the pristine and Y^{3+}-doped systems were derived from the frequency-dependent complex dielectric function, $\varepsilon(\omega) = \varepsilon_1(\omega) + i\varepsilon_2(\omega)$, within the independent-particle approximation (IPA) using the sum-over-states approach. Here, $\varepsilon(\omega)$ denotes the dielectric function, where the imaginary part, $\varepsilon_2(\omega)$, is associated with dielectric energy loss or light absorption, while the real part, $\varepsilon_1(\omega)$, relates to the energy stored within the material. To ensure an accurate description of the high-energy optical response, a sufficiently large number of unoccupied bands (NBANDS = 600) were included in the calculations. The optical bandgap was extracted from the $\varepsilon_2(\omega)$ spectrum. In doped conducting systems, the optical response features two distinct components: a low-energy Drude peak attributed to free-carrier intraband transitions and a high-energy absorption edge stemming from interband transitions. Notably, the optical bandgap was defined as the photon energy at which $\varepsilon_2(\omega)$ surpasses a threshold value of 0.1.

3 Results and discussion

3.1 Preparation and characterization of $Mg_2Al_4Si_5O_{18}$

The phases and thermal properties of the samples were identified using XRD and TG-DSC, respectively. Figure 1(a) displays the XRD patterns of samples annealed at 1200, 1300, and 1400 °C for 4 h. The ceramics are crystallized to the intermediate forsterite (Mg_2SiO_4) phase at 1200 °C and spinel ($MgAl_2O_4$) phase at 1300 °C. Subsequently, as the reaction temperature increased, all the intermediate phases disappeared, and $Mg_2Al_4Si_5O_{18}$ was synthesized.

The TG-DSC results of the raw materials are shown in Fig. 1(b). It can be seen from the TG curves that the temperature range of 450–530 °C corresponds to the desorption of structural water within γ-AlOOH and the transformation into an alumina intermediate phase (Reaction (1)):

$$2AlOOH \rightarrow (2-v)/2H_2O + Al_2O_{3-v/2}(OH)_v \quad (1)$$

followed by the elimination of residual hydroxyl groups in the mesophase of alumina (Reaction (2)):

$$Al_2O_{3-v/2}(OH)_v \rightarrow v/2H_2O + Al_2O_3 \quad (2)$$

As shown in Fig. 1(b), the DSC curve exhibits four types of peaks. A_1 is the endothermic broad peak at approximately 500 °C, A_2 and A_3 are two exothermic peaks at approximately 1250 °C, and A_4 is the melting endothermic peak at 1430 °C. The peak at 1200–1300 °C corresponds to forsterite Mg_2SiO_4 [47] and spinel $MgAl_2O_4$ [48] (Eqs. (3) and (4)):

$$MgO + Al_2O_3 = MgAl_2O_4 \quad (3)$$

$$2MgO + SiO_2 = Mg_2SiO_4 \quad (4)$$

At 1400 °C, the target product $Mg_2Al_4Si_5O_{18}$ is formed (Eq. (5)):

$$Mg_2SiO_4 + 2MgAl_2O_4 + 9SiO_2 + 2Al_2O_3 = 2Mg_2Al_4Si_5O_{18} \quad (5)$$

In Fig. 1(c), high-angle annular dark-field scanning transmission electron microscopy (HAADF-STEM) images and EDS elemental mapping confirm the presence of Mg, Al, and Si in the single $Mg_2Al_4Si_5O_{18}$. Figure 1(d) depicts the crystal structure of β-$Mg_2Al_4Si_5O_{18}$, which belongs to the orthorhombic crystal system (space group *Cccm*) and contains four molecules per unit cell. Mg^{2+} is six-coordinated by O^{2-} ions, forming a distorted [MgO_6] octahedron. Both Si^{4+} and Al^{3+} are in fourfold coordination, forming [SiO_4] and [AlO_4] tetrahedra, respectively. These tetrahedra, together with [MgO_6] octahedra, constitute the crystal framework [49]. The tetrahedra are of two types: T_2 tetrahedra, which form twisted hexagonal rings with a 30° twist between adjacent layers via corner sharing, and T_1 tetrahedra, which are connected to adjacent T_2 rings and share two opposite edges with [MgO_6] octahedra. The magnesium atoms are located within these distorted [MgO_6] octahedra, each of which shares edges with three T_1 tetrahedra [50]. Figure 1(e) displays the calculated vis-NIR solar reflectance and mid-infrared emittance spectra of $Mg_2Al_4Si_5O_{18}$. In this work, R^* was quantified according to ASTM standards E891-87, G159-878, and G173-03 using the method detailed in Eq. (6):

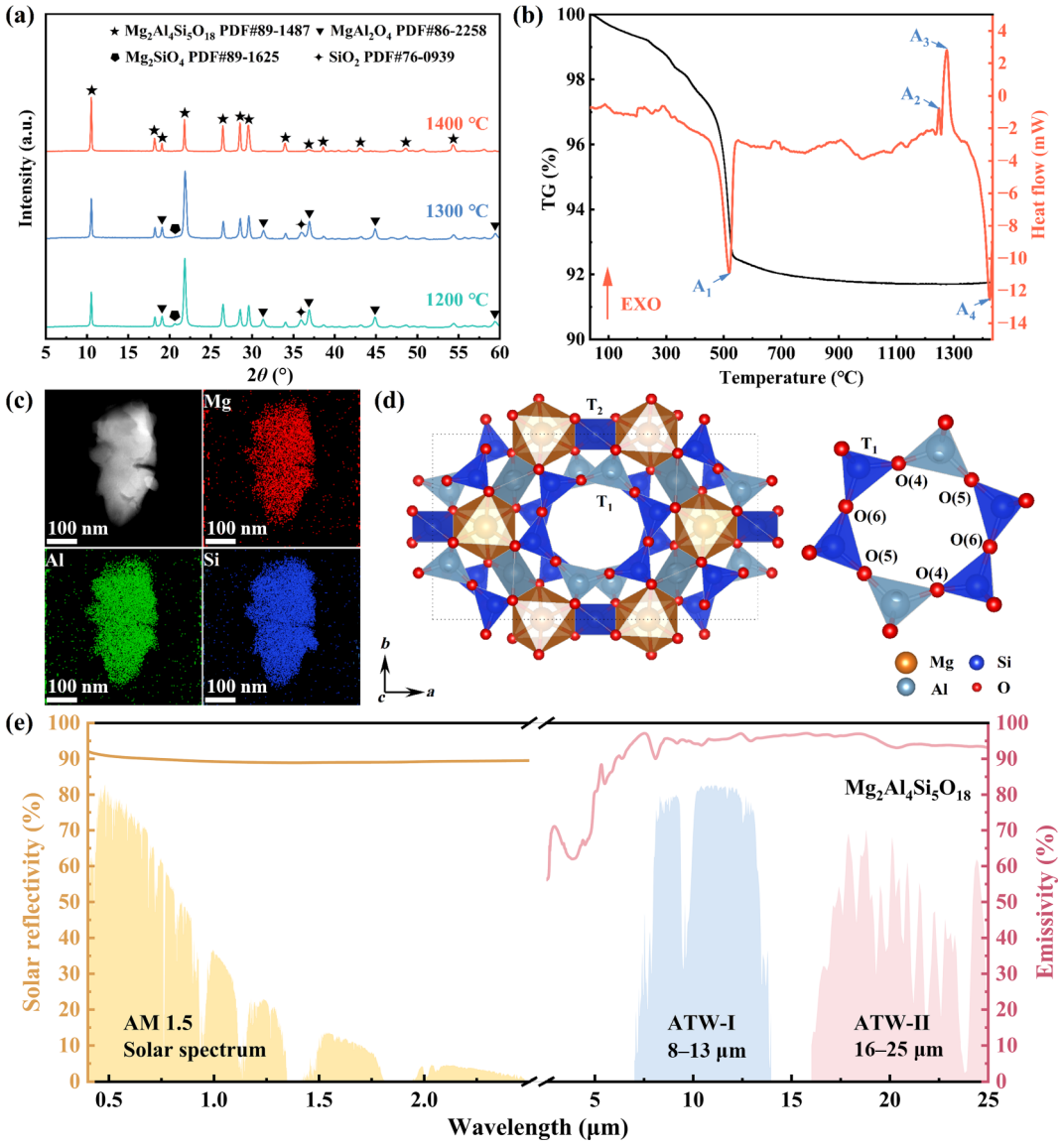

Fig. 1 Preparation and characterization of $Mg_2Al_4Si_5O_{18}$. (a) XRD patterns of raw materials thermally treated at different annealing temperatures for 4 h. (b) TG-DSC curves of raw materials. (c) HAADF images and corresponding elemental distribution mappings. (d) Crystal structure of β-$Mg_2Al_4Si_5O_{18}$. (e) Spectral reflectance and emissivity of β-$Mg_2Al_4Si_5O_{18}$.

$$R^* = \frac{\int_{0.4}^{2.5} r(\lambda)\, i(\lambda)\, \mathrm{d}\lambda}{\int_{0.4}^{2.5} i(\lambda)\, \mathrm{d}\lambda} \tag{6}$$

where $r(\lambda)$ is the experimentally measured spectral reflectance ($W{\cdot}m^{-2}$), and $i(\lambda)$ is the solar spectral irradiance ($W{\cdot}m^{-2}{\cdot}nm^{-1}$). Similarly, the average emissivity of the sample in the first atmospheric window (8–13 μm) was calculated using Eq. (7):

$$\varepsilon_1 = \frac{\int_8^{13} I_{bb}(T,\lambda)\, \varepsilon(\lambda)\, \mathrm{d}\lambda}{\int_8^{13} I_{bb}(T,\lambda)\, \mathrm{d}\lambda} \tag{7}$$

The average emissivity of the sample in the second atmospheric window (16–25 μm) was given by Eq. (8):

$$\varepsilon_2 = \frac{\int_{16}^{25} I_{bb}(T,\lambda)\, \varepsilon(\lambda)\, \mathrm{d}\lambda}{\int_{16}^{25} I_{bb}(T,\lambda)\, \mathrm{d}\lambda} \tag{8}$$

where $I_{bb}(T, \lambda)$ denotes the blackbody radiation intensity, and $\varepsilon(\lambda)$ represents the experimentally measured spectral emittance of the sample (λ being the wavelength). The value of $I_{bb}(T, \lambda)$ [10] can be calculated from Eq. (9):

$$I_{bb}(T,\lambda) = \frac{4\pi c^2 h}{\lambda^5} \frac{1}{e^{\frac{2\pi hc}{\lambda k_B T}} - 1} \tag{9}$$

where c, h, k_B, and T are the speed of light (3×10^8 $m{\cdot}s^{-1}$), the reduced Planck constant (1.055×10^{-34} $J{\cdot}s$), the Boltzmann constant (1.381×10^{-23} $J{\cdot}K^{-1}$), and the ambient temperature (300 K), respectively.

The as-prepared samples exhibit a high ATW average emissivity of 94.39% in ATW-I and 96.02% in ATW-II, along with a high average reflectivity of 89.52% in vis-NIR. The material exhibits high solar reflectivity in the vis-NIR regions owing to its wide bandgap, which effectively suppresses photon absorption. Concurrently, the stretching and bending vibrations of Al–O and Si–O bonds within the [AlO_4] and [SiO_4] tetrahedral units endow the material with high emissivity. The emissivity of $Mg_2Al_4Si_5O_{18}$ exhibits a decline at approximately 8 μm (90.46%) and 20 μm

(92.90%), which is attributed to phonon-polariton resonance arising from the strong interaction between optical phonons and photons. This phenomenon results in a highly reflective (low-emissivity) spectral regime, which is detrimental to radiative cooling performance. To overcome these intrinsic limitations and further tailor the spectral characteristics of $Mg_2Al_4Si_5O_{18}$, we propose a targeted improvement strategy that leverages both bandgap and phonon engineering.

3.2 Material optimization

To simultaneously suppress the phonon-polariton resonance while maintaining a large bandgap, we first employ DFT to calculate the PDOS at specific atomic sites. Subsequently, the impact of doping on the optical bandgap is predicted through the computation of the dielectric function.

As shown in Fig. 2, the PDOS was calculated for different atomic sites, with the vibrational modes analyzed in detail. Figure 2(a) reveals that the optical modes in the frequency range of 4–14 THz (21–75 μm) are predominantly contributed by Mg atoms, whereas the modes above 14 THz are mainly attributed to the vibrations of Al and Si atoms. For $Mg_2Al_4Si_5O_{18}$, the Mg atoms predominantly contribute to the low-frequency regime (< 10 THz) [21]. Within the spectral range, phonons possess insufficient vibrational energy to excite internal thermal radiation effectively. As illustrated in Fig. 2(c), the total and partial PDOS of the Y^{3+}-doped $Mg_2Al_4Si_5O_{18}$ exhibit differences compared to those in Fig. 2(a). In Fig. 2(c), the characteristic peaks associated with T_1 and T_2 exhibit pronounced broadening and a concomitant reduction in intensity. This peak broadening directly reflects the disruption of the original ordered lattice structure induced by Y^{3+} doping.

Figure 2(b) illustrates the vibrational behavior of O atoms in the Mg-bonding environment of the pristine sample, and Fig. 2(d) depicts the altered bonding environment of O atoms after Y^{3+} doping. The doping of Y^{3+} breaks the lattice symmetry and changes the local bonding environment [43]. These changes increase lattice disorder and shorten the phonon lifetime, thereby causing the vibration modes to split and the spectral lines to broaden [51]. This also generates additional vibrational peaks within the ATW-I (37.5–23.08 THz) and ATW-II (18.74–12.0 THz) frequency ranges. The doping of Y^{3+} introduces lattice disorder, which weakens the local field and reduces the phonon polarizability [52]. This leads to a broadening of the phonon spectral lines, indicating a decrease in the coherence of phonon

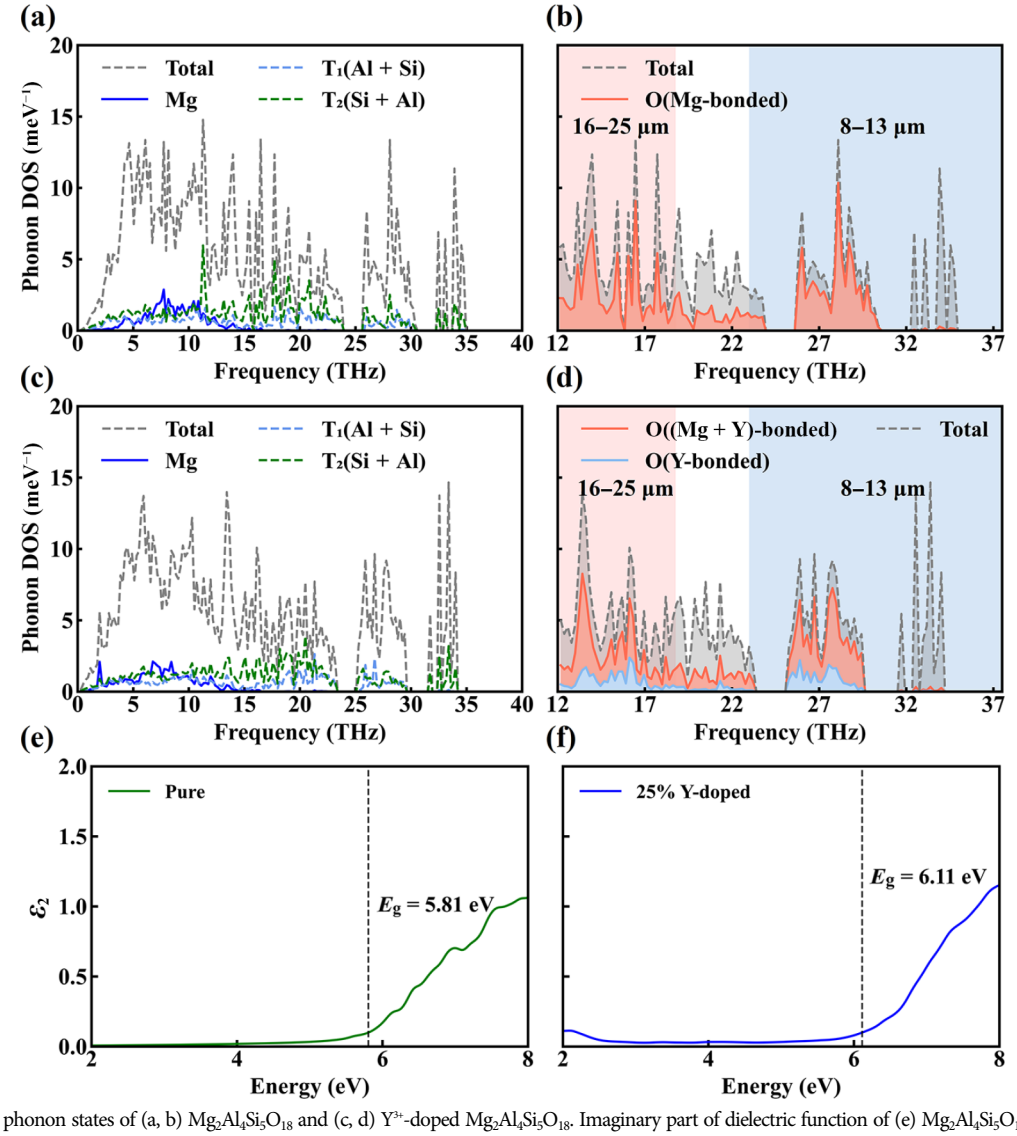

Fig. 2 Density of phonon states of (a, b) $Mg_2Al_4Si_5O_{18}$ and (c, d) Y^{3+}-doped $Mg_2Al_4Si_5O_{18}$. Imaginary part of dielectric function of (e) $Mg_2Al_4Si_5O_{18}$ and (f) Y^{3+}-doped $Mg_2Al_4Si_5O_{18}$.

清華大学出版社 Tsinghua University Press | SciOpen

vibrations. Consequently, the material exhibits reduced reflectivity and enhanced ATW emissivity.

The oxygen PDOS exhibits enhanced continuity and higher peak intensities across both the ATW-I and ATW-II ranges. This indicates a greater number of active vibrational modes available for excitation in these spectral bands. As shown in Fig. 2(d), Y^{3+} doping leads to a significant increase in the integrated total PDOS. The trend suggests that the material possesses a higher density of phonon modes capable of excitation. This enhancement is evidenced by the increased intensity of vibrational modes in the phonon spectrum and the optimized PDOS, resulting in a significant improvement in ATW emissivity.

The modulation of the bandgap induced by Y^{3+} doping constitutes the key factor in optimizing solar reflectance. The imaginary part ($\varepsilon_2(\omega)$) of the dielectric function is intimately linked to optical absorption, corresponding to interband electronic transitions from occupied states near the Fermi level in the valence band to unoccupied states in the conduction band [53]. Typically, the bandgap corresponds to the onset energy where the $\varepsilon_2(\omega)$ curve exhibits a significant rise. In this work, the optical bandgap is defined as the photon energy at which $\varepsilon_2(\omega)$ exceeds the threshold value of 0.1. As shown in Fig. 2(e), the bandgap of $Mg_2Al_4Si_5O_{18}$ is approximately 5.81 eV. The bandgap exhibits a slight broadening to 6.11 eV with Y^{3+} doping (Fig. 2(f)). This result substantiates that Y^{3+} doping effectively tailors the photon absorption threshold, thereby achieving bandgap broadening.

Taking into account both the broadened phonon spectrum and the widened bandgap, Y^{3+} emerges as the most promising dopant to suppress solar absorption while enhancing emissivity within the ATW. Consequently, Y^{3+}-doped $Mg_2Al_4Si_5O_{18}$ will stand out as a prime candidate for high-performance, eco-friendly, low-cost radiative cooling ceramics.

3.3 Phase composition and microstructure of Y^{3+}-doped $Mg_2Al_4Si_5O_{18}$

Building upon the preliminary material optimization, Y^{3+}-doped $Mg_2Al_4Si_5O_{18}$ was successfully synthesized through an improved fabrication process and optimized doping ratios, thereby incorporating the aforementioned phonon and bandgap engineering strategies. Figure 3 presents the XRD patterns of $Mg_2Al_4Si_5O_{18}$:xY^{3+} (x = 0%, 2.5%, 5%, 7.5%, 10%, and 12.5%) ceramics synthesized via the high-temperature solid-state reaction method. Figure 3 shows that all samples within the solid solution range (0% ≤ x ≤ 10%) exhibit a single-phase β-cordierite structure (PDF#89-1487), with no diffraction peaks from impurity phases detected. The solid solution limit is reached at x = 12.5%, where a secondary phase (Al_2SiO_5) appears. Among the three cationic sites, Mg^{2+} (ionic radius: 0.72 Å), Al^{3+} (0.39 Å), and Si^{3+} (0.26 Å), steric hindrance dictates that the Mg^{2+} site is the most likely location for Y^{3+} (0.90 Å) to occupy. According to Ci *et al.* [54], the Mg^{2+} ions in $Mg_2Al_4Si_5O_{18}$ can be substituted by larger cations such as Dy^{3+} (0.91 Å), Sm^{3+} (0.96 Å) [55], and Ca^{2+} (1.00 Å) [56] to form solid solutions. Consequently, the incorporation of Y^{3+} into the Mg^{2+} site of $Mg_2Al_4Si_5O_{18}$ is thermodynamically favorable. Furthermore, $Mg_2Al_4Si_5O_{18}$ can accommodate cation vacancies [57]. As illustrated in Fig. 3, compared with the single-component $Mg_2Al_4Si_5O_{18}$, the characteristic diffraction peak shifts to higher angles with increasing Y^{3+} doping concentration. The shift in the diffraction peak is attributed to lattice contraction [58]. The lattice contraction results from the formation of cation vacancies, which are generated to maintain charge neutrality in response to the excess positive charge introduced when Y^{3+} ions substitute into Mg^{2+} sites.

Figure 4 exhibits the experimental, simulated, and difference Rietveld refinement XRD patterns for $Mg_2Al_4Si_5O_{18}$:xY^{3+} (x = 0%, 2.5%, 5%, 7.5%, and 10%). The calculated XRD pattern shows good agreement with the experimental data. The Rietveld refinement results for the $Mg_2Al_4Si_5O_{18}$:xY^{3+} (x = 0%, 2.5%, 5%, 7.5%, and 10%) ceramics are summarized in Fig. 4(f). Both the lattice parameter a and the unit cell volume (V) decrease as the doping concentration (x) increases from 0% to 10%. The observed contraction indirectly confirms the dominant role of cation vacancies, which is consistent with the trends revealed by the XRD patterns.

HAADF-STEM images and corresponding elemental distribution mapping for the $Mg_2Al_4Si_5O_{18}$:xY^{3+} (x = 2.5%, 5%, 7.5%, and 10%) samples are presented in Figs. 5(a)–5(d). A uniform elemental distribution at the nanoscale is observed in all samples, with no signs of elemental segregation or depletion. High-resolution transmission electron microscopy (HRTEM) further analyzed the crystal structure, as shown in Figs. 5(e)–5(h). For the samples with x = 2.5%, 5%, 7.5%, and 10%, the measured (100) interplanar spacings are 0.858, 0.849, 0.845, and 0.829 nm, respectively. The above discussion confirms that $Mg_2Al_4Si_5O_{18}$:xY^{3+} (x = 2.5%, 5%, 7.5%, and 10%) is a homogeneous single-phase solid solution. The lattice variation can be attributed to lattice contraction induced by cationic vacancies, which is consistent with the XRD analysis.

3.4 ATW emissive performance of Y^{3+}-doped $Mg_2Al_4Si_5O_{18}$

Figures 6(a) and 6(b) show the emissivity of $Mg_2Al_4Si_5O_{18}$:xY^{3+} (x = 0%, 2.5%, 5%, 7.5%, and 10%) powders in the ATW-I and ATW-II bands, respectively. The emissivities of $Mg_2Al_4Si_5O_{18}$ in the ATW-I and ATW-II bands are 94.39% and 96.02%, respectively. The average emissivity values were calculated according to Eqs. (7) and (8). The high ATW emissivity of $Mg_2Al_4Si_5O_{18}$ can be attributed to its crystal structure, which features diverse phonon vibrational modes such as stretching and bending vibrations of Si–O and Al–O bonds. With increasing Y^{3+} doping concentration, the average emissivity monotonically increases, reaching 97.53% for ATW-I and 98.39% for ATW-II at x = 10%. Notably, with increasing Y^{3+} doping concentration, the emissivity dips at approximately 8 and 20 μm are effectively mitigated, increasing from 90.46% to 95.42% and from 92.90% to 97.67%, respectively. The enhanced emissivity is primarily due to the synergistic effect of lattice distortion and the activation of localized phonon modes. Specifically, the Y^{3+} doping-induced lattice distortion, by breaking crystal symmetry and introducing local strain, not only activates local phonon modes but also

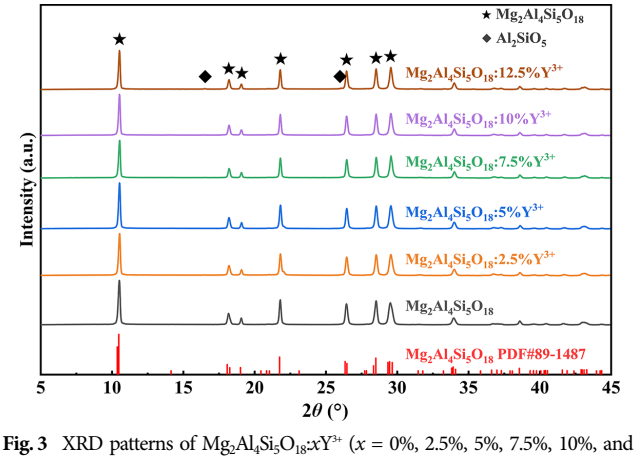

Fig. 3 XRD patterns of $Mg_2Al_4Si_5O_{18}$:xY^{3+} (x = 0%, 2.5%, 5%, 7.5%, 10%, and 12.5%), together with the standard pattern obtained from PDF#89-1487.

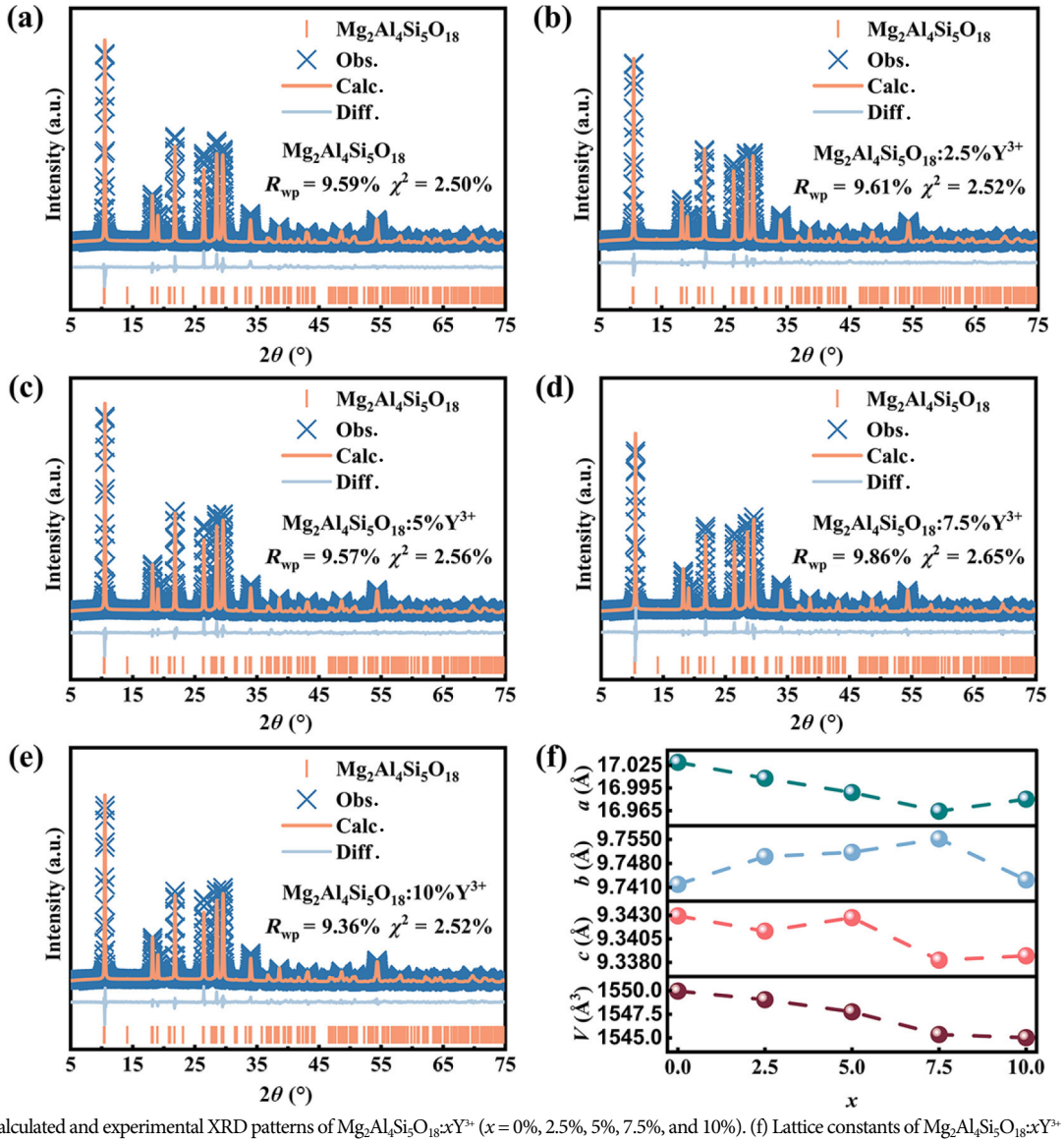

Fig. 4 (a–e) Calculated and experimental XRD patterns of $Mg_2Al_4Si_5O_{18}$:xY^{3+} (x = 0%, 2.5%, 5%, 7.5%, and 10%). (f) Lattice constants of $Mg_2Al_4Si_5O_{18}$:xY^{3+} (x = 0%, 2.5%, 5%, 7.5%, and 10%).

broadens the phonon spectrum. This essentially increases the PDOS available for infrared emission within the ATW band, thereby leading to an enhancement in emissivity.

The vibrational modes and the degree of lattice distortion were systematically analyzed and characterized. Figure 7 shows the Raman spectra of $Mg_2Al_4Si_5O_{18}$:xY^{3+} (x = 0%, 2.5%, 5%, 7.5%, and 10%) in the wavenumber range of 500–1200 cm^{-1}. Based on group theory calculations, the spinel structure with space group *Cccm* exhibits 174 vibrational modes [59], and the vibrational symmetry representation is shown in Eq. (10):

$$\Gamma_{total} = 23A_g + 25B_{1g} + 19B_{2g} + 20B_{3g} + 17A_u + 19B_{1u} + 25B_{2u} + 26B_{3u} \quad (10)$$

Among these, 87g modes are Raman-active, while 67u modes are infrared-active [21]. The peak near 672 cm^{-1} corresponds to the stretching vibration of the Al–O bond. Peaks within the range of 565–576 cm^{-1} are assigned to bending vibrations of Al–O and Si–O bonds and to the stretching vibrations of Mg–O bonds [55]. The peaks at 974, 1012, and 1186 cm^{-1} are attributed to the stretching vibrations of Si–O bonds [59]. These diverse phonon vibrational modes provide a crucial structural foundation for achieving high emissivity within the atmospheric window in $Mg_2Al_4Si_5O_{18}$:xY^{3+} (x = 0%, 2.5%, 5%, 7.5%, and 10%), consistent with our PDOS results. With increasing Y^{3+} doping concentration, the Raman bands at 555 and 576 cm^{-1} exhibit a gradual blueshift. This phenomenon is attributed to lattice contraction, which is induced by the increasing concentration of cationic vacancies resulting from Y^{3+} substitution. The introduction of these vacancies triggers a contraction of the surrounding Al/Si–O bonds, which reduces the lattice constant and ultimately accounts for the observed peak shift. Therefore, Raman spectroscopy characterization was employed to directly monitor the changes in phonon vibration modes induced by Y^{3+} doping. The observed peak blueshift and broadening confirm the occurrence of lattice distortion, which enhances phonon activity by breaking crystal symmetry. This provides critical vibrational evidence for the enhancement of emissivity in the ATW band.

To further quantify the lattice distortion, we calculated the standard deviation (σ_i) of the bond angles within the [$(Si_4Al_2)O_{18}$] hexagonal rings (Table 1). The bond angles listed in Table 1 (e.g., O5–O4–O6, O4–O6–O5, O6–O5–O4) were derived from the crystal structure data obtained after Rietveld refinement. In cordierite, the bending of these rings is a critical measure of

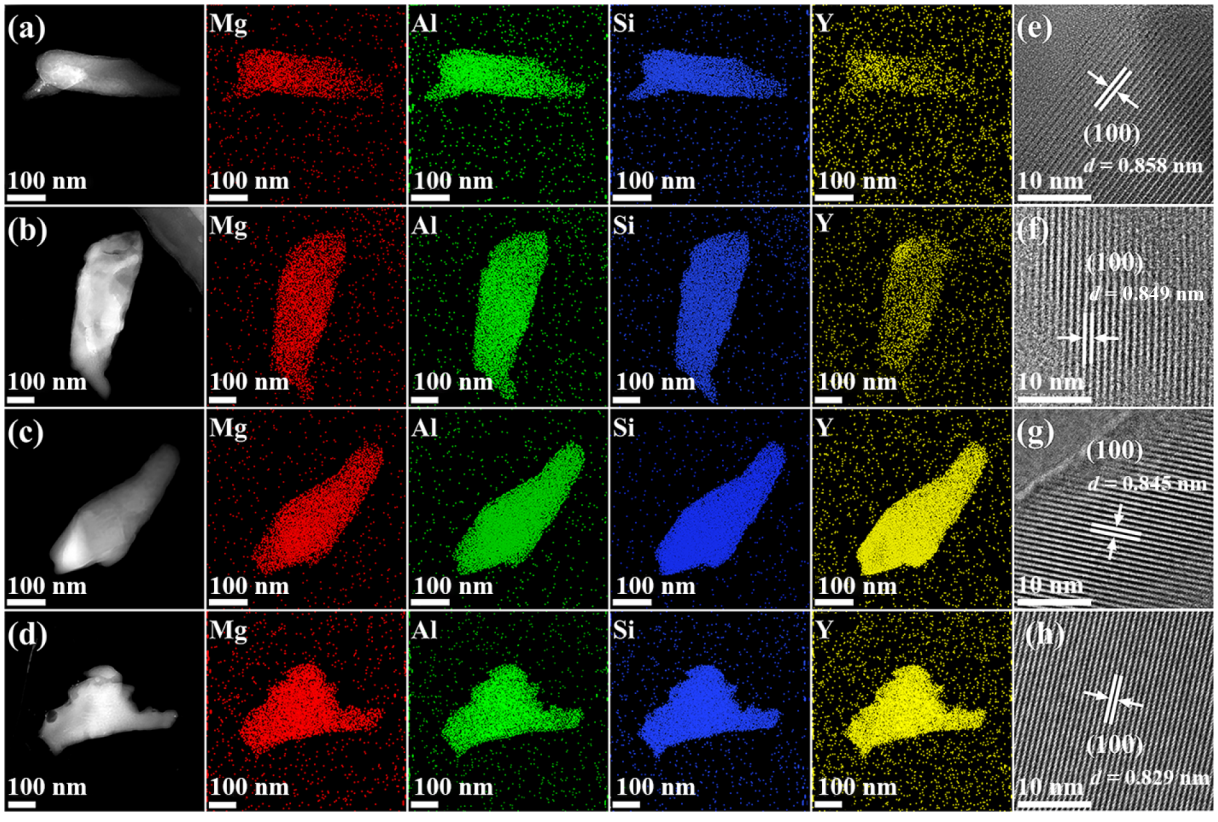

Fig. 5 (a–d) HAADF images and corresponding elemental distribution mappings. (e–h) HRTEM images of $Mg_2Al_4Si_5O_{18}$:xY^{3+} (x = 2.5%, 5%, 7.5%, and 10%).

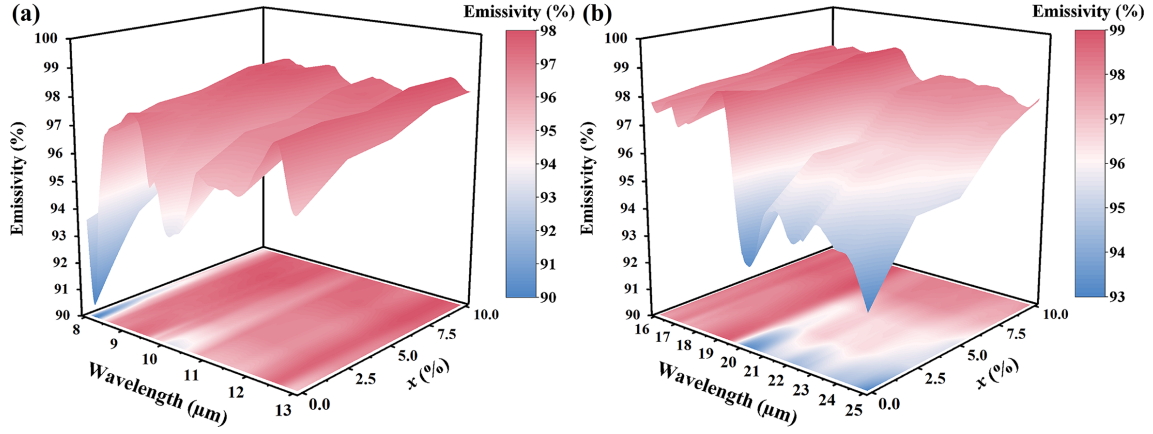

Fig. 6 Emissivity spectrum of $Mg_2Al_4Si_5O_{18}$:xY^{3+} (x = 0%, 2.5%, 5%, 7.5%, and 10%) at (a) 8–13 μm and (b) 16–25 μm.

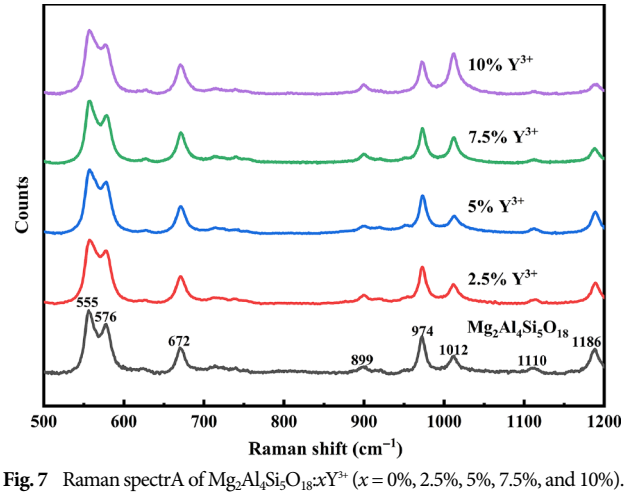

Fig. 7 Raman spectrA of $Mg_2Al_4Si_5O_{18}$:xY^{3+} (x = 0%, 2.5%, 5%, 7.5%, and 10%).

central symmetry. A lower σ_i signifies a ring structure closer to an ideal, higher-order hexagon [55]. Since doping induces lattice distortion and perturbs crystal symmetry, the degree of lattice distortion can be effectively quantified by monitoring the variations in characteristic bond angles within the hexagonal rings. Based on the equal diagonal lengths of the rings, σ_i was of $Mg_2Al_4Si_5O_{18}$:xY^{3+} (x = 0%, 2.5%, 5%, 7.5%, and 10%) ceramics by using Eq. (11):

$$\sigma_i = \sqrt{\frac{\left[(A546 - 120^\circ)^2 + (A465 - 120^\circ)^2 + (A654 - 120^\circ)^2\right]}{6}} \tag{11}$$

where $A546$ denotes the O(5)–O(4)–O(6) bond angle, as shown in Fig. 1(d). The same applies to $A465$ and $A654$. The σ_i values of $Mg_2Al_4Si_5O_{18}$:xY^{3+} (x = 0%, 2.5%, 5%, 7.5%, and 10%) were calculated to be 6.10, 7.33, 9.85, 10.28, and 10.33, respectively. This

indicates that the incorporation of Y^{3+} induces lattice distortion, thereby perturbing the symmetry of the crystal. This distortion is consistent with the previously observed broadening of the phonon spectrum and the blueshift of the Raman bands.

Figures 8(a) and 8(b) further illustrate the correlation between lattice distortion (σ_i) and ATW emissivity. As the degree of σ_i increases from 6.5 to 9.5, the ATW emissivity correspondingly rises. Combined with PDOS analysis, the disparity in ionic radii induces lattice distortion, thereby compromising crystal symmetry and enhancing lattice vibrational activity and absorption [60,61]. By disrupting the phonon modes responsible for reflection within the Reststrahlen band [62], this distortion effectively suppresses phonon polariton resonance, thereby optimizing the material for ATW radiative cooling performance. The experimental trends are in excellent agreement with the simulation predictions. In summary, lattice distortion regulates the phonon vibrational behavior, and the optimized phonon spectral characteristics ultimately realize the enhancement of ATW emissive performance.

Table 1 Bond angles of $Mg_2Al_4Si_5O_{18}$:xY^{3+}

Bond angle	x = 0%	x = 2.5%	x = 5%	x = 7.5%	x = 10%
O(5)–O(4)–O(6) (°)	128.3	130.2	133.6	133.7	134.1
O(4)–O(6)–O (5) (°)	113.8	116.5	110.7	108.9	109.7
O(6)–O(5)–O(4) (°)	117.9	113.3	115.6	117.3	116.1

3.5 Vis-NIR solar reflectance performance of Y^{3+}-doped $Mg_2Al_4Si_5O_{18}$

The vis-NIR spectrum spanning (0.4–2.5 μm) accounts for approximately 95% of the total solar irradiance. For PRC ceramics, high vis-NIR solar reflectance (R^*) [63] is essential to minimize solar heat gain and achieve efficient cooling performance. As shown in Fig. 9(a), the average vis-NIR reflectance of pure $Mg_2Al_4Si_5O_{18}$ is 89.52%. With Y^{3+} doping at x = 10%, this value increases significantly to 94.77%. The average solar reflectance was calculated using Eq. (6). The enhanced reflectivity stems predominantly from the combined contribution of two fundamental parameters, the bandgap and the electronic polarizability. As the bandgap (E_g) [64] dictates the intrinsic absorption edge and $Mg_2Al_4Si_5O_{18}$ possesses a direct band gap, the evolution upon doping was investigated using Eq. (12) [65]:

$$ahv^2 = A\,(hv - E_g) \tag{12}$$

where a is the absorption coefficient, h is the Planck constant, v is the acoustic frequency, and A is a constant.

Further characterization confirmed that Y^{3+}-doped $Mg_2Al_4Si_5O_{18}$ exhibits a wider bandgap than $Mg_2Al_4Si_5O_{18}$, in agreement with DFT-guided predictions. The variation in the optical E_g with doping concentration, plotted in Fig. 9(b), confirms the aforementioned correlation. As shown, the E_g of undoped $Mg_2Al_4Si_5O_{18}$ is 3.35 eV. It increases progressively with

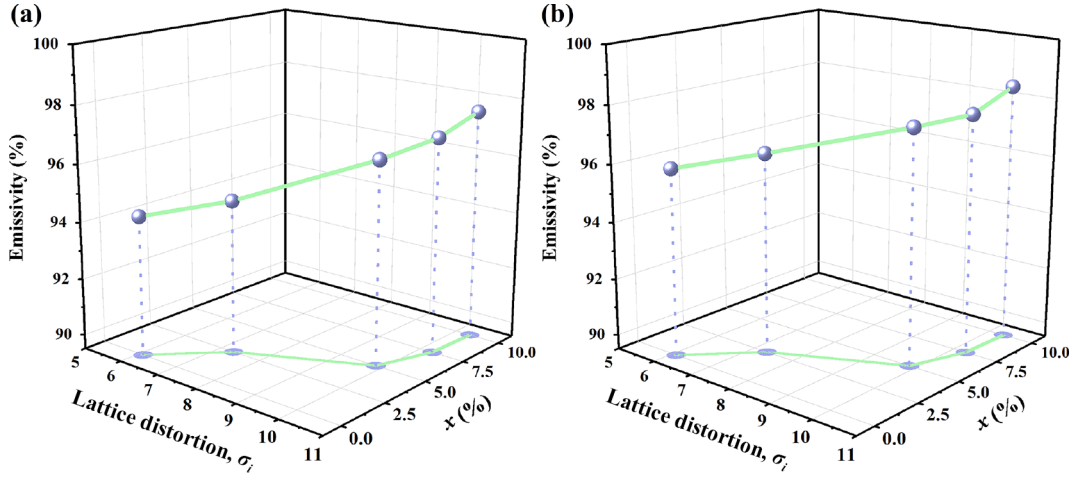

Fig. 8 Relationship between emissivity in (a) ATW-I, (b) ATW-II, doping concentration (x), and lattice distortion (σ_i).

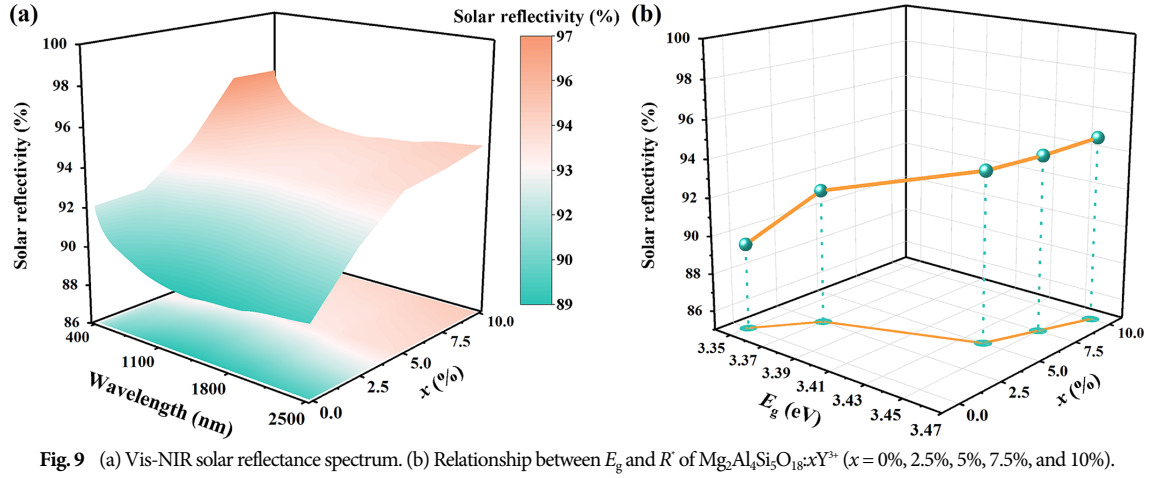

Fig. 9 (a) Vis-NIR solar reflectance spectrum. (b) Relationship between E_g and R^* of $Mg_2Al_4Si_5O_{18}$:xY^{3+} (x = 0%, 2.5%, 5%, 7.5%, and 10%).

清華大学出版社 Tsinghua University Press | SciOpen

higher Y^{3+} doping, reaching 3.46 eV at x = 10%. The Y^{3+} electronic transition demands high excitation energy, resulting in pronounced optical inertness [42]. This characteristic effectively preserves the integrity and stability of the intrinsic electronic band structure, thereby inducing bandgap widening.

Additionally, the dielectric function of a material, which governs the vis-NIR reflectivity, originates from the electronic polarization response. The dielectric response of materials primarily arises from polarization induced by the electromagnetic field. When the electromagnetic wave propagates through the medium, the time-varying electric field induces dielectric polarization, the process described by the constitutive relations in Maxwell's theory (Eq. (13)) [66]:

$$\boldsymbol{D} = \varepsilon \boldsymbol{E} + \boldsymbol{P} = (1 + \chi)\,\varepsilon_0 \boldsymbol{E} = \varepsilon_0 \varepsilon_r \boldsymbol{E} \tag{13}$$

where $\boldsymbol{D}$ is the electric displacement vector (C·m^{-2}), $\boldsymbol{E}$ is the electric field intensity (V·m^{-2}), $\boldsymbol{P}$ is the polarization intensity (C·m^{-2}), χ is the electric polarizability, ε is the dielectric constant, ε_0 is the vacuum dielectric constant, and ε_r is the relative complex permittivity. In the vis-NIR band, the dielectric response of the material is dominated by electronic polarization (P_e). The contribution from ionic polarization (P_i) is negligible because ions cannot respond sufficiently fast to the rapidly oscillating electromagnetic field at these frequencies. Within the framework of the Lorentz oscillator model [66], the complex dielectric function of the material in this frequency range is given by Eqs. (14) and (15):

$$\varepsilon_r(\omega) = 1 + \frac{\boldsymbol{P}_e}{\varepsilon_0 \boldsymbol{E}} \tag{14}$$

$$R = \left| \frac{\sqrt{\varepsilon_r} - 1}{\sqrt{\varepsilon_r} + 1} \right|^2 \tag{15}$$

This relationship directly connects the microscopic behavior of electron polarization to the macroscopic dielectric constant. The real and imaginary parts of the dielectric constant, as governed by electromagnetic wave transmission theory (e.g., the Fresnel formula [67] in Eq. (15)), subsequently determine the reflectivity. Therefore, the electron polarization characteristics in the vis-NIR band constitute the core microscopic mechanism that regulates the dielectric response and the overall reflection behavior.

In summary, the enhanced vis-NIR reflectance is attributed to the concerted modulation of E_g and electronic polarization. Specifically, Y^{3+} doping widens the bandgap via stabilization of the electronic structure, minimizing optical absorption within the target spectrum. Concurrently, the induced electronic polarizability governs the dielectric response, which correlates with macroscopic permittivity to regulate electromagnetic wave transport and reflection. This synergistic action across electronic and polarization dimensions significantly boosts reflectance, establishing the core microtheoretical basis for efficient radiative cooling in PRC ceramics.

3.6 PRC performance assessment

To process and analyze the experimental results, the net cooling power of $Mg_2Al_4Si_5O_{18}$:10% Y^{3+} was calculated by comprehensively accounting for all relevant thermal factors.

$$P_{net}(T) = P_{rad}(T) - P_{atm}(T_{amb}) - P_{sun} - P_{conv+cond} \tag{16}$$

where T and T_{atm} are the surface temperatures of the material and ambient air, $P_{net}(T)$ is the net cooling power, $P_{rad}(T)$ is the power radiated out by the cooler at temperature T, and P_{sun} and P_{atm} (T_{amb}) are the absorbed solar power and the absorbed downward atmospheric thermal radiation at T_{amb}. $P_{conv+cond}$ is the nonradiative power. Based on the above model and the measured optical properties, the calculated net radiative cooling power of the material is ~113.1 W·m^{-2}. The synthesized $Mg_2Al_4Si_5O_{18}$:10% Y^{3+} ceramics in this work demonstrate superior net radiative cooling power compared to previously reported MgO and Al_2O_3-based composites as well as SiO_2-based cooling ceramics. It achieves an exceptional value of 113.1 W·m^{-2}, significantly outperforming oxide systems such as polydimethylsiloxane (PDMS)/Al_2O_3 [68] (65.10 W·m^{-2}), MgO [69] (102.70 W·m^{-2}), Al_2O_3-polyvinylidene fluoride (PVDF) [70] (96.70 W·m^{-2}), PDMS-SiO_2 [71] (63.2 W·m^{-2}), Al_2O_3-$BaSO_4$-cementitious pastes [72] (78.34 W·m^{-2}), and fluorine modification of poly ether ether ketone (FPEEK)/PVDF-Hexafluoropropylene (HFP)/SiO_2 [73] (78.70 W·m^{-2}).

To explore the potential application of $Mg_2Al_4Si_5O_{18}$:10% Y^{3+} as a radiant cooling coating, a series of outdoor simulation experiments was designed and executed, drawing inspiration from the pioneering radiative "cooling glass" strategy reported in Zhao *et al.* [44]. $Mg_2Al_4Si_5O_{18}$:10% Y^{3+} particles were compounded with low-melting point glass, and the composite was thermally treated to adhere to slate substrates, yielding a scalable and durable coating. Figure 10(a) illustrates the outdoor experimental setup employed for real-time temperature monitoring of coated and uncoated slate samples under natural solar irradiation. The experimental apparatus consists of aluminum foil, polystyrene, a PE film, and a K-type thermocouple (Fig. 10(b)). As illustrated in Fig. 11, under solar irradiation at 12:42 PM, the temperature of the space covered by bare slate reached 63.4 °C, whereas the coated substrate exhibited a significantly lower temperature of 46.9 °C. This substantial temperature difference of 16.5 °C demonstrates the effective radiative cooling performance. Such superior cooling capability can be attributed to the radiative cooling property of

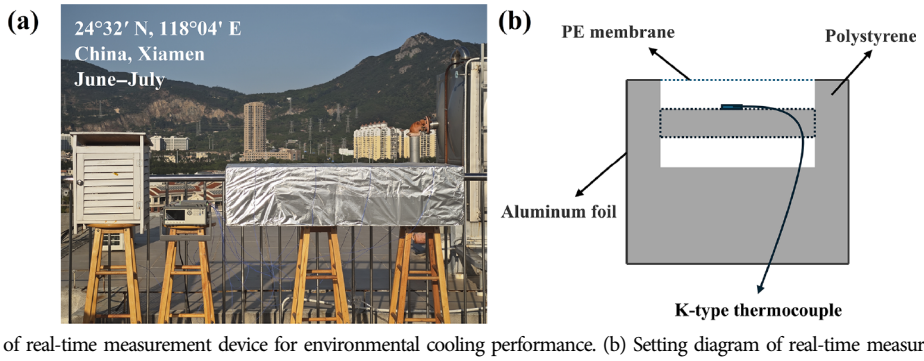

Fig. 10 (a) Photograph of real-time measurement device for environmental cooling performance. (b) Setting diagram of real-time measurement of environmental cooling performance is drawn.

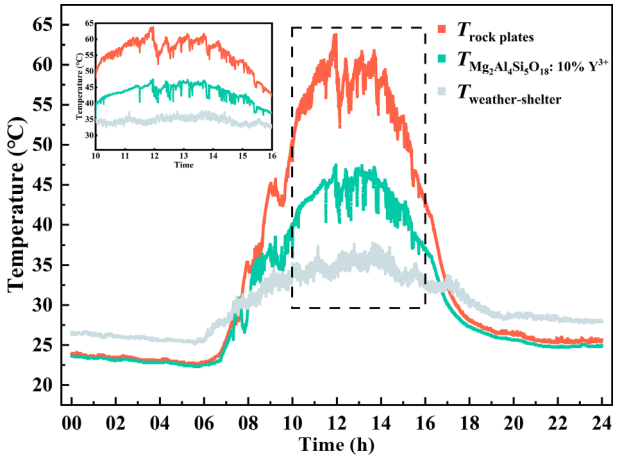

Fig. 11 24 h passive radiation cooling performance curve of $Mg_2Al_4Si_5O_{18}$:10% Y^{3+}.

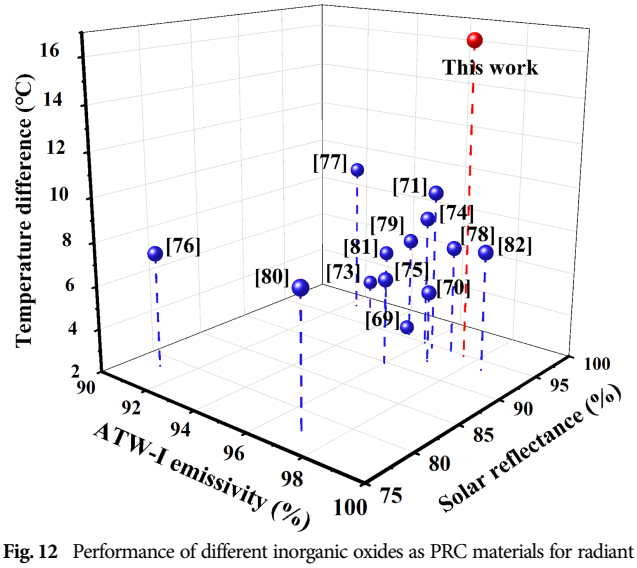

Fig. 12 Performance of different inorganic oxides as PRC materials for radiant coolers. These include $SiO_2/BaSO_4$ [74], TiO_2/glass MPs [75], aluminum ceramic fiber-based ceramic matrix composites (ACF-CMC) [76], SiO_2/PVA [77], MgO [69], $CaCO_3$/silica gel/Al_2O_3 [78], $BaSO_4$/bacterial cellulose [79], Al_2O_3/PVDF [70], PTFE/SiO_2@Cotton [80], $Al_2O_3/BaSO_4$/cementitious pastes [71], CNF/CNC/TiO_2 [81], FPEEK/PVDF-HFP/SiO_2 [73], and PDMS/CNFs/nano-SiO_2 [82].

$Mg_2Al_4Si_5O_{18}$:10% Y^{3+}, coupled with the rich infrared-active vibrational modes within the low-melting point glass matrix.

Figure 12 compares the vis-NIR reflectivity, ATW-I emissivity, and temperature difference of the $Mg_2Al_4Si_5O_{18}$:10% Y^{3+} coating with various PRC materials. As shown in Fig. 12, most reported radiative cooling materials are polymer-based composites. While these materials exhibit acceptable optical performance in specific spectral bands, their intrinsic poor weather resistance and weak UV aging resistance severely [44] restrict long-term stability in complex outdoor environments. In contrast, the $Mg_2Al_4Si_5O_{18}$:10% Y^{3+} coating developed in this work achieves a synergistic optimization of high solar reflectance and infrared emissivity. First, the raw material system consists of low-cost and earth-abundant elements. The inexpensive basic components avoid the use of costly noble metals (such as indium or silver), thereby controlling material costs at the source. Second, the synthesis and coating processes are feasible and scalable for mass production. The ceramic powder is synthesized via a mature high-temperature solid-state reaction method, which is simple to operate. The coating preparation involves mixing the ceramic powder with low-melting-point glass to form a slurry, followed by coating and sintering. This is a straightforward process. By employing a rare-earth ion doping strategy, we construct a radiative cooling system that combines high solar reflectance with dual ATW infrared emission. This approach also offers low-cost fabrication, exceptional radiative cooling performance, and superior practical cooling capability.

This technical approach not only provides a long-term stable passive cooling solution for outdoor applications such as buildings and photovoltaic modules but also effectively reduces the energy consumption of active cooling systems (e.g., air conditioners), thereby cutting carbon emissions and contributing to energy conservation and sustainable development under the "carbon peak" and "carbon neutrality" targets. Furthermore, the doping modification strategy based on inorganic functional ceramics breaks the performance bottlenecks of traditional polymer-based cooling materials, opening a new pathway for the large-scale outdoor application of radiative cooling technology. It is projected to play a pivotal role in mitigating global climate change and provide core material support for the construction of low-carbon, resilient urban infrastructure.

4 Conclusions

In this work, based on DFT calculations that guided the rational doping process, a series of high-performance $Mg_2Al_4Si_5O_{18}$:xY^{3+} (x = 0%, 2.5%, 5%, 7.5%, and 10%) PRC ceramics were synthesized via synergistic optimization of phonon and bandgap engineering. This strategy not only enhanced the bandgap energy but also effectively suppressed the phonon-polariton resonance. Specifically, Y^{3+} doping regulates lattice distortion to optimize phonon vibration and thus enhance emissivity while simultaneously optimizing the bandgap and improving electronic polarizability, which synergistically contributes to the increase in reflectance. The average emissivity of the ATW-I of $Mg_2Al_4Si_5O_{18}$:xY^{3+} (x = 0%, 2.5%, 5%, 7.5%, and 10%) ceramics rose from 94.39% to 97.53%, while that in the ATW-II band increased from 96.02% to 98.39%. Meanwhile, the average reflectance of the vis-NIR region increased from 89.52% to 94.77%. The E_g widened from 3.35 to 3.46 eV, indicating that the doping strategy effectively improved the PRC performance of $Mg_2Al_4Si_5O_{18}$:xY^{3+} (x = 0%, 2.5%, 5%, 7.5%, and 10%) ceramics. In addition, under sunlight irradiation, the PRC coating achieved a maximum temperature reduction of 16.5 °C and a net PRC power of ~113.1 $W{\cdot}m^{-2}$. This work overcomes the performance limitations of pure β-$Mg_2Al_4Si_5O_{18}$, offering an environmentally friendly, low-cost, and highly stable ceramic PRC material and providing new insights into sustainable passive cooling technology.

Acknowledgements

This research was supported by the National Natural Science Foundation of China (No. 52402093), the Self-deployment Project Research Programs of Haixi Institutes, Chinese Academy of Sciences (No. CXZX-2023-JQ07), the XMIREM Autonomously Deployment Project (No. 2023GG03), the Natural Science Foundation of Xiamen (Nos. 3502Z202472048 and 3502Z202573100), and the Outstanding Youth Fund of Henan Province (No. 252300421006).

Availability of data and materials

The data that support the findings of this study are available from the corresponding author upon reasonable request.

Competing interests

The authors have no competing interests to declare that are relevant to the content of this article.

References

[1] Lin KX, Chen SR, Zeng YJ, *et al.* Hierarchically structured passive radiative cooling ceramic with high solar reflectivity. *Science* 2023, **382**: 691–697.

[2] Jaramillo-Fernandez J, Whitworth GL, Pariente JA, *et al.* A self-assembled 2D thermofunctional material for radiative cooling. *Small* 2019, **15**: 1905290.

[3] Xie F, Jin WL, Nolen JR, *et al.* Subambient daytime radiative cooling of vertical surfaces. *Science* 2024, **386**: 788–794.

[4] Yang KJ, Wu XK, Zhou L, *et al.* Towards practical applications of radiative cooling. *Nat Rev Clean Technol* 2025, **1**: 235–254.

[5] Tang KC, Dong KC, Li JC, *et al.* Temperature-adaptive radiative coating for all-season household thermal regulation. *Science* 2021, **374**: 1504–1509.

[6] Wang SC, Jiang TY, Meng Y, *et al.* Scalable thermochromic smart windows with passive radiative cooling regulation. *Science* 2021, **374**: 1501–1504.

[7] Heo SY, Lee GJ, Kim DH, *et al.* A Janus emitter for passive heat release from enclosures. *Sci Adv* 2020, **6**: 1906.

[8] Zhao X, Tang GH. 0D/2D co-doping network enhancing thermal conductivity of radiative cooling film for electronic device thermal management. *ACS Appl Mater Inter* 2024, **16**: 37853–37864.

[9] Song XK, Gong H, Li HC, *et al.* Molecularly and structurally designed polyimide nanofiber radiative cooling films for spacecraft thermal management. *Adv Funct Mater* 2025, **35**: 2413191.

[10] Wu XK, Li JL, Xie F, *et al.* A dual-selective thermal emitter with enhanced subambient radiative cooling performance. *Nat Commun* 2024, **15**: 815.

[11] Lin CJ, Li KQ, Li M, *et al.* Pushing radiative cooling technology to real applications. *Adv Mater* 2025, **37**: 2409738.

[12] Yang S, Tang SZ, Yuan XY, *et al.* Advances in tunable radiative cooling materials: Design, mechanisms, and applications. *Adv Funct Mater* 2026, **36**: 11552.

[13] Tian ZY, Zhang K, Tong XY, *et al.* Scalable dry-processing of ceramic-polymer composite flexible passive daytime radiative cooling films. *Chem Eng J* 2026, **535**: 175153.

[14] Jiang S, Jiang SQ, Yan JT, *et al.* Large-scale continuous production of cellulose/hollow SiO_2 composite aerogel fibers for outdoor all-day radiation cooling. *Nano Energy* 2025, **136**: 110688.

[15] Han WB, Kang HS, Heo SY, *et al.* Stretchable and biodegradable composite films for disposable, antibacterial, radiative cooling system. *Chem Eng J* 2024, **483**: 149388.

[16] Chen DC, Hwang CW, Chang CY, *et al.* Superdurable, flexible ceramic nanofibers for sustainable passive radiative cooling. *ACS Nano* 2025, **19**: 28280–28294.

[17] Liu H, Zhu SN. Hierarchical-morphology metafabric for scalable passive daytime radiative cooling. *Science* 2021, **66**: 3787–3790.

[18] Jung Y, Kim JS, Bang J, *et al.* Energy-saving window for versatile multimode of radiative cooling, energy harvesting, and defrosting functionalities. *Nano Energy* 2024, **129**: 110004.

[19] Kim S, Lee S, Lee J, *et al.* Passive isothermal film with self-switchable radiative cooling-driven water sorption layer for arid climate applications. *Nat Commun* 2024, **15**: 8000.

[20] Jing Y, Chen QJ, Sui MY, *et al.* The first principles calculation and temperature-sensitive luminescence behavior of optimized red phosphor $Mg_2Al_4Si_5O_{18}$:Eu^{3+}. *J Lumin* 2017, **181**: 49–55.

[21] Li YR, Tian ZL, Luo YX, *et al.* Pressure-induced low-lying phonon modes softening and enhanced thermal resistance in β-$Mg_2Al_4Si_5O_{18}$. *Phys Rev B* 2017, **95**: 054301.

[22] Chen GL, Wang YM, Qiu J, *et al.* Robust inorganic daytime radiative cooling coating based on a phosphate geopolymer. *ACS Appl Mater Inter* 2020, **12**: 54963–54971.

[23] Li YY, Yin YC, Bai Y, *et al.* Engineering the optical properties of $SrZrO_3$ crystals via Zn doping for superior passive daytime radiative cooling. *J Adv Ceram* 2025, **14**: 9221107.

[24] Dang SC, Xiang JB, Yao HX, *et al.* Color-preserving daytime passive radiative cooling based on Fe^{3+}-doped $Y_2Ce_2O_7$. *Energ Buildings* 2022, **259**: 111861.

[25] Ma MT, Huang MZ, Xue LY, *et al.* A potential thermophotovoltaic emitter $Er(Ta_{1-x}Nb_x)O_4$ ($0 \le x \le 0.2$) with excellent selective emission performance. *J Adv Ceram* 2025, **14**: 9221072.

[26] Xu Y, Wang GP, Yang BB, *et al.* La-doped $Bi_4Ti_3O_{12}$ nanosheets: Ferroelectric polarization-enhanced carrier dynamics for efficient tetracycline photodegradation. *J Adv Ceram* 2026, **15**: 9221248.

[27] Pang T, Lin SS, You FL, *et al.* Synergistic enhancement of crystallinity and transparency in Tb^{3+}-doped nano-glass-ceramics for high-resolution X-ray imaging. *J Adv Ceram* 2025, **14**: 9221122.

[28] Jiang MR, Qi N, Mao YF, *et al.* Realizing intense deep-far-red broadband emission derived from mica ceramics through isomorphic cation substitution/doping for plant cultivation lighting and latent fingerprint identification. *J Adv Ceram* 2026, **15**: 9221254.

[29] Liu BH, He CY, Li Y, *et al.* Quasi-metallic high-entropy spinel oxides for full-spectrum solar energy harvesting. *Matter* 2024, **7**: 140–157.

[30] Ouyang Y, Jiang XX, Jiang F, *et al.* Light-soaking induced optical tuning in rare earth-doped all-inorganic perovskite. *Adv. Funct Mater* 2022, **32**: 2107086.

[31] Liu CL, Huang XT, Zhu J, *et al.* Exploiting structural benefit of double phosphate for extremely efficient near-ultraviolet light towards multiple functionality. *J Adv Ceram* 2025, **14**: 9221131.

[32] Wang SM, Kuang FH, Yan QZ, *et al.* Crystallization and infrared radiation properties of iron ion doped cordierite glass-ceramics. *J Alloys Compd* 2011, **509**: 2819–2823.

[33] Wang YJ, Pan X, Liu ZQ, *et al.* Self-reduction-induced Mn heterovalent coexistence for vis-NIR dual-emission. *J Adv Ceram* 2025, **14**: 9221118.

[34] He CY, Li Y, Zhou ZH, *et al.* High-entropy photothermal materials. *Adv Mater* 2024, **36**: 2400920.

[35] Zhao P, Dong M, Liu X, *et al.* Ultrahigh thermal robustness of high-entropy spectrally selective absorbers for next-generation concentrated solar power system. *Adv Funct Mater* 2024, **34**: 2411316.

[36] Du PY, Wei Y, Liang Y, *et al.* Near-infrared-responsive rare earth nanoparticles for optical imaging and wireless phototherapy. *Adv Sci* 2024, **11**: 2305308.

[37] Fan Y, Bai YL, He XD, *et al.* Revealing corrosion mechanisms and enabling predictive lifetime assessment of high-entropy rare-earth disilicates with superior CMAS corrosion resistance. *J Adv Ceram* 2026, **15**: 9221251.

[38] Chen GL, Xie EY, Sun YF, *et al.* High-strength micron-thick layered ceramics with ultralow radiation transmittance for thermal shielding above 1273 K. *Adv Funct Mater* 2026, **36**: 12733.

[39] Wang C, Sun GT, He CY, *et al.* Entropy-driven multiphase engineering enables superior broadband infrared emissivity in high-entropy oxides. *Adv Mater* 2026, **38**: 08636.

[40] Yun Y, Buragohain P, Li M, *et al.* Intrinsic ferroelectricity in Y-doped HfO_2 thin films. *Nat Mater* 2022, **21**: 903–909.

[41] Jiang Y, Ferhat M, Fan WH, *et al.* Thermoelectric enhancement achieved by Y and La co-doping in n-type $Mg_{3.2}Sb_{1.5}Bi_{0.5}$. *Chem Eng J* 2022, **446**: 136981.

[42] Shilpa CK, Jasira SV, Veena VP, *et al.* Thermally stable Sm^{3+} doped $SrCeO_3$ single-phase white phosphor with Y^{3+} sensitization for fabricating wLEDs. *Sci Rep-UK* 2025, **15**: 24205.

[43] Lin H, Xu DK, Li AM, *et al.* Facile synthesis and emission enhancement in $NaLuF_4$ upconversion nano/microcrystals via Y^{3+} doping. *Sci Rep-UK* 2017, **7**: 13762.

[44] Zhao XP, Li TY, Xie H, *et al.* A solution-processed radiative cooling glass. *Science* 2023, **382**: 684–691.

[45] Kresse G, Furthmüller J. Efficiency of *ab-initio* total energy calculations for metals and semiconductors using a plane-wave basis set. *Comput Mater Sci* 1996, **6**: 15–50.
[46] Gonze X, Lee C. Dynamical matrices, Born effective charges, dielectric permittivity tensors, and interatomic force constants from density-functional perturbation theory. *Phys Rev B* 1997, **55**: 10355–10368.
[47] Zhang LQ, Lai YM, Xiang PW, *et al.* Entropy-driven phase evolution and enhanced temperature stability in low-temperature sintering Mg_2SiO_4-based ceramics. *Ceram Int* 2025, **51**: 64442–64451.
[48] Omkaram I, Buddhudu S. Photoluminescence properties of $MgAl_2O_4$: Dy^{3+} powder phosphor. *Opt Mater* 2009, **32**: 8–11.
[49] Wei DL, Seo HJ. Determination of phase-formation of $(Mg_{1-x}Mn_x)_2Al_4Si_5O_{18}$ (x = 0–1) cordierite solid-solutions via crystallographic sites and luminescence dynamics of Mn^{2+} centers. *J Mater Chem C* 2020, **8**: 7899–7907.
[50] Li YR, Wang JM, Wang JY. Approaching extremely low thermal conductivity by crystal structure engineering in $Mg_2Al_4Si_5O_{18}$. *J Mater Res* 2015, **30**: 3729–3739.
[51] Galaviz P, Portwin KA, Yu DH, *et al.* Phonon density of states of magnetite (Fe_3O_4) nanoparticles via molecular dynamics simulations. *Comput Mater Sci* 2026, **261**: 114293.
[52] Adamus P, Xu B, Marsik P, *et al.* Analogies of phonon anomalies and electronic gap features in the infrared response of $Sr_{14-x}Ca_xCu_{24}O_{41}$ and underdoped $YBa_2Cu_3O_{6+x}$. *Rep Prog Phys* 2023, **86**: 044502.
[53] Mondal AK, Mohamed MA, Ping LK, *et al.* First-principles studies for electronic structure and optical properties of p-type calcium doped α-Ga_2O_3. *Materials* 2021, **14**: 604.
[54] Ci ZP, Sun QS, Qin SC, *et al.* Warm white light generation from a single phase Dy^{3+} doped $Mg_2Al_4Si_5O_{18}$ phosphor for white UV-LEDs. *Phys Chem Chem Phys* 2014, **16**: 11597–11602.
[55] Song KX, Liu P, Lin HX, *et al.* Symmetry of hexagonal ring and microwave dielectric properties of $(Mg_{1-x}Ln_x)_2Al_4Si_5O_{18+x}$ (Ln = La, Sm) cordierite-type ceramics. *J Eur Ceram Soc* 2016, **36**: 1167–1175.
[56] Vepa SSVSS, Umarji AM. Effect of substitution of Ca on thermal expansion of cordierite ($Mg_2Al_4Si_5O_{18}$). *J Am Ceram Soc* 1993, **76**: 1873–1876.
[57] Chen J, Liu YG, Liu HK, *et al.* The luminescence properties of novel α-$Mg_2Al_4Si_5O_{18}$:Eu^{2+} phosphor prepared in air. *RSC Adv* 2014, **4**: 18234–18239.
[58] Chen GL, Xie EY, Zhao QY, *et al.* Dual phonon–photon scattering in randomized tantalate-niobate duplex ceramics for > 1273 K thermal shielding. *Acta Mater* 2026, **305**: 121788.
[59] Lang ZD, Ren LC, Shao PC, *et al.* $(Cu_{0.5}Ti_{0.5})_{3+}$-doped cordierite ceramics with near-zero τ_f and low ε_r for temperature-stable microwave dielectrics. *Ceram Int* 2025, **51**: 24952–24959.
[60] Chen T, He YY, Pan YY, *et al.* High-entropy rare earth stannate ceramics: Acid corrosion resistant radiative cooling materials with high atmospheric transparency window emissivity and high near-infrared solar reflectivity. *J Adv Ceram* 2024, **13**: 630–640.
[61] Wang WM, Liu BH, He CY, *et al.* High-entropy engineering for broadband infrared radiation. *Adv Funct Mater* 2023, **33**: 2303197.
[62] Liu BY, Wang ZY, Zheng Y, *et al.* Suppressing reflectance in Reststrahlen bands of $Cu_{0.64}Cr_{1.51}Mn_{(0.85-x)}Co_xO_4$ to achieving broadband high emissivity via phonon vibration modes coupling. *Mater Today Phys* 2025, **51**: 101649.
[63] Jose S, Joshy D, Narendranath SB, *et al.* Recent advances in infrared reflective inorganic pigments. *Sol Energy Mat Sol C* 2019, **194**: 7–27.
[64] Zhu HL, Liu L, Xiang HM, *et al.* Improved thermal stability and infrared emissivity of high-entropy $REMgAl_{11}O_{19}$ and $LaMAl_{11}O_{19}$ (RE = La, Nd, Gd, Sm, Pr, Dy; M = Mg, Fe, Co, Ni, Zn). *J Mater Sci Technol* 2022, **104**: 131–144.
[65] Yuan XL, Wang QH, Wu RK, *et al.* Environment-friendly Ca^{2+}/Cr^{3+} co-doping $LaAlO_3$ ceramics with excellent infrared radiation performance for energy-saving. *J Adv Ceram* 2025, **14**: 9221017.
[66] Hilfiker JN, Tiwald T. *Spectroscopic Ellipsometry for Photovoltaics*. Cham (Switzerland): Springer International Publishing, 2018.
[67] Norman GE, Saitov IM, Stegailov VV. First-principles calculation of the reflectance of shock-compressed xenon. *J Exp Theor Phys+* 2015, **120**: 894–904.
[68] Park C, Park C, Park S, *et al.* Hybrid emitters with raspberry-like hollow SiO_2 spheres for passive daytime radiative cooling. *Chem Eng J* 2023, **459**: 141652.
[69] Wang XF, Liu DQ, Wan Z, *et al.* A gradient nanoporous radiative cooling ceramic with high spectral selectivity. *Chem Eng J* 2024, **500**: 157344.
[70] Yang XX, Yang YL, Chen LT, *et al.* A switchable dual-mode film with designed intercalated and hierarchical structures for highly efficient passive radiation cooling and solar heating. *Chem Eng J* 2024, **494**: 152920.
[71] Park C, Lee W, Park C, *et al.* Efficient thermal management and all-season energy harvesting using adaptive radiative cooling and a thermoelectric power generator. *J Energy Chem* 2023, **84**: 496–501.
[72] Hu Y, Guo T, Qu XY, *et al.* Enhanced passive radiative cooling of cementitious composites for efficient photovoltaic thermal management. *Energ Convers Manage* 2025, **344**: 120268.
[73] Bai YG, Xie L, Gu YX, *et al.* The best of both worlds—A flexible composite film with hierarchical porous structure for sustainable energy harvesting and passive radiative cooling. *J Mater Sci Technol* 2026, **260**: 124–135.
[74] Cheng ZM, Han H, Wang FQ, *et al.* Efficient radiative cooling coating with biomimetic human skin wrinkle structure. *Nano Energy* 2021, **89**: 106377.
[75] Xue X, Qiu M, Li YW, *et al.* Creating an eco-friendly building coating with smart subambient radiative cooling. *Adv Mater* 2020, **32**: 1906751.
[76] Cheng YY, Chen YJ, Hu XY, *et al.* Ceramic matrix composites as self-standing monoliths and coatings for thermal superinsulation and passive daytime radiative cooling. *Adv Funct Mater* 2025, **35**: 2504931.
[77] Li HL, Li X, Pan MY, *et al.* Flexible ceramic radiative cooling membranes with high reflectivity in solar spectrum, excellent UV and fire resistance. *Adv Funct Mater* 2026, **36**: 16949.
[78] Xu XG, Wang N, Li X, *et al.* A novel carbonated inorganic radiative cooling material and its spectral manipulation mechanism. *Chem Eng J* 2025, **517**: 164444.
[79] Ding Y, Wu LD, Lu X, *et al.* A sustainable and robust Janus film Inspired by the bird's nest structure for efficient year-round outdoor thermal management. *Chem Eng J* 2024, **500**: 156918.
[80] Zhang LX, Xu B, Zhou M, *et al.* Excellent durability and multifunctional textiles with dual-mode evaporative and radiative cooling enabled by *in-situ* growth of SiO_2 and electrostatic network coating. *Chem Eng J* 2025, **522**: 168259.
[81] Yang T, Guo SY, Zhao X, *et al.* Scalable, binder-free, ultrathin, and outdoor stable passive cooling paints engineered by cellulose-weaved topological scattering network. *J Energy Chem* 2026, **115**: 584–594.
[82] Ren CY, Wei ZC, Wang JW, *et al.* Bioinspired superhydrophobic cellulose-based thermal emitters with multiphase scattering structure for durable daytime radiative cooling. *Nano Energy* 2025, **141**: 111076.